doi:10.20944/preprints202111.0544.v1

Article

Enhanced Mach-Zehnder Interferometer Multimode–Single-Mode–Multimode Fiber Optic Refractive Index Sensor Based on Surface Plasmon Resonance

Zahra Akbarpour [1], Vahid Ahmadi [1,*] and Farzaneh Arabpour Roghabadi [2]

[1] Optoelectronics and Nanophotonics Research Group, Faculty of Electrical and Computer Engineering, Tarbiat Modares University, Tehran, Iran; zahraakbarpour@modares.ac.ir (Z.A.); v_ahmadi@modares.ac.ir (V.A.)
[2] Faculty of Chemical Engineering, Tarbiat Modares University, Tehran, Iran; arabpour@modares.ac.ir
* Correspondence: v_ahmadi@modares.ac.ir

Abstract: In this paper, an all-fiber Mach-Zehnder interferometer (MZI) sensor for refractive index (RI) measuring is presented, which is based on Multimode–Single-mode–Multimode (MSM) fiber. The effects of both reducing the radius of the sensing part and the surface plasmon resonance (SPR) on its efficiency are investigated. Increasing the interaction of high-order modes with external media, caused by etching the cladding layer of the single-mode fiber part, significantly improves the sensitivity. Both wavelength and intensity interrogation approaches are employed to study the Multimode–etched Single-mode–Multimode (MESM) fiber sensor. The intensity and the wavelength sensitivities for the RI measurement in the range of 1.428-1.458 are obtained as -2308.92 %/RIU and 1313.14 nm/RIU, respectively. Finally, the MESM-SPR sensor is proposed and characterized. Results exhibit high performance in the RI range of 1.333 to 1.357, in which the sensitivity of 1433 nm/RIU is achieved. The advantages like low cost, high sensitivity, and simple fabrication methods make these sensors promising devices for chemical, food industry, and biosensing applications.

Keywords: Fiber optic sensor; Refractive index; Mach-Zehnder; Surface plasmon resonance; Etching

1. Introduction

Researchers have uncovered that fiber optics not only are utilized as a communication tool and a low-loss waveguide to convey light signals, but also have been widely employed for sensing applications in the last four decades. A large number of theses and papers in the field of fiber optic sensing indicate yet there is a considerable capacity for investigation and improvement. This kind of sensor has attracted remarkable attention due to its advantages, including high sensitivity, low weight, miniature size, high precision, electromagnetic immunity, high-temperature range, and a variety of structures [1,2]. Making a fiber optic sensitive requires modifying its structure along with allowing the propagating light to interact with the outside media. By doing so, it has the ability to measure any variation in the expected parameter. Therefore, according to what parameter is the purpose of measurement, the sensor is designed and fabricated with an appropriate fiber structure. Fluid refractive index (RI), temperature, strain, gas density in a chamber, water impurities, humidity, and electromagnetic field are the elements that can be measured by fiber optic sensors (FOSs) [3]. Since any alteration in the measuring parameter can modify the characteristics of the guided lightwave inside the fiber, the performance analysis of an FOS can be accomplished by the modulation of phase, intensity, polarization, or wavelength [4]. Due to the ease of creating variation in the phase and intensity of light within the fiber, the first two methods are commonly used for sensing analysis. Phase modulation method-based fiber sensors mainly include structures operating on the basis of phase change between modes, for instance, Fabry-Perot and Mach-Zehnder interferometer (MZI), which are the most well-known structures in this category. MZI configurations are superior and more reliable owing to their simplicity, high sensitivity, and structural diversity. The main structures in the category of MZI configuration-based FOSs are based on: a sandwiched thin core (TC)-photonic crystal (PC) fiber [5], a TC-PC-TC fiber connected between two single-mode fibers (SMFs) [6], an asymmetric microfiber [7], an in-line multimode–single-mode–multimode (MSM) [8], a single-mode–multimode–single-mode(SMS) fiber in which the first end of the multimode fiber (MMF) is tapered [9], an embedded four-core fiber between two SMFs [10], and an in-line MMF-etched multicore fiber-MMF [11]. The propagating light is not thoroughly confined in these sensors, and the evanescent waves (EWs) penetrate the surrounding media. The phase difference between the fundamental mode and higher-order modes changes by any variation in the environment, resulting in a wavelength shift of the output spectrum.

In order to increase the possibility of light interaction with the environment, reducing the fiber diameter in the sensitive area of the structure using chemical, polishing, or thermal methods can be employed [12,13]. Applying the surface plasmon resonance (SPR) property in FOS has also been significantly effective in improving the sensor performance, which can be provided by deposition of a thin film of metals such as gold or silver on the fiber surface [14]. If the propagation constant of surface plasmons (SPs) matches the propagation constant of the incident photons, a part of the signal energy is transformed to the electrons, causing the resonance of SPs [15,16]. By using this approach, the penetration depth of the field in the external environment is increased. As the dielectric constants of both metal and dielectric are involved in resonance conditions, the central wavelength changes with the dielectric constant of the sensing part [17]. The optical fiber-based SPR sensors do not have the drawbacks of the prism-based ones, such as its disability of remote sensing and lots of mechanical as well as optical parts. Instead, they have the advantages of high sensitivity and compact size [18].

Since RI sensing is of great importance in the areas like food industry, biosensing, detecting water impurities, and petroleum industry, various FOS structures have been reported [19,20]. In 2016, Wang et al. presented an RI sensor based on a single-mode–PC–single-mode (SM-PC-SM) fiber structure in which fused points were tapered up to a diameter of 60.4µm. The acquired sensitivity in the RI range of 1.3333 to 1.3737 was 260.8 nm/RIU [21]. In 2017, Ding et al. reported a tapered coreless fiber structure to measure the RI using the SPR sensing mechanism. A thin film of 40 nm Au thickness was deposited on one side of the tapered section. When the RI varied from 1.3864 to 1.416, the sensitivity of 866.1 nm/RIU was obtained [12]. In 2019, Haifeng et al. investigated the effect of chemical etching on the performance of the SM-PC-SM fiber sensor. The RI sensitivity was improved by decreasing the cladding diameter, and the value of 359.37 nm/RIU within the range of 1.333 – 1.381 was obtained [22]. In 2020, Zhang et al. presented an MSM fiber sensor and tapered the SMF section up to 50µm diameter to gain a high RI sensitivity. The sensitivity of 1879.87 nm/RIU under RI of 1.437 was achieved [23].

In this paper, we offer an SPR-based MSM sensor and investigate the effects of reducing the waist of the sensing region and SPR phenomenon on its performance. The main body of the sensor is fabricated by inserting a segment of an SMF between two MMFs, then etching and Au film coating operations are performed. Due to the hetero-core structure, high-order modes are excited in the SMF cladding, resulting in the formation of the MZI configuration. Applying the SPR effect to the MZI structure, the cladding of which is partially removed makes this RI sensor high performance. The analysis of the sensor behavior is accomplished based on the inter-mode interference. Also, the effects of different lengths of the SMF section and thicknesses of the gold layer are examined on the output spectrum.

2. Sensing Principle and Fabrication

The schematic diagram of the proposed multimode–etched single-mode–multimode (MESM) structure is illustrated in Figure 1. An SMF segment is inserted between two MMFs, resulting in core diameter-mismatches at the connection points. The input field is divided into two parts as soon as it reaches the first joint; the fundamental mode enters the core of the SMF and the rest of the light wave penetrates the cladding, leading to the excitation of high-order modes. After propagating along the SMF and reaching the second joint, cladding modes overlay the core mode, resulting in an interference pattern. I_o, the intensity of the transmitted wave, is calculated as [11,24]:

$$I_o = I_{core} + \sum_m I_{cl}^m + \sum_m \sqrt{2 I_{core} I_{cl}^m} \cos\underbrace{\left(2\pi\Delta n_{eff}^m \, {}^{l}\!/_{\lambda}\right)}_{\beta_m} \tag{1}$$

The optical paths in this structure are similar to the arms of the Mach-Zehnder, except that both arms are embedded in the same fiber. I_{core}, I_{cl}^m, and β_m refer to the intensity of the core mode, m-th order cladding mode, and the optical phase difference between them, respectively. λ is the signal wavelength, l is the length of the SMF section, and $\Delta n_{eff}^m = n_{core,eff} - n_{cl,eff}^m$ corresponds to the difference between the effective RI of the fundamental and m-order modes. If the condition of $\beta_m = (2m+1)\pi$ occurs, the intensity of the output light will be minimized at some wavelengths which correspond to the positions of the valleys in the interference spectrum. λ_m, the wavelength of the valleys, is given by [5,25]:

$$\lambda_m = \frac{2\Delta n_{eff}^m l}{2m+1} \quad ; \quad m = 1, 2, 3, \cdots \tag{2}$$

Regarding this equation, we find that only parameters that have the essential effect on λ_m are Δn_{eff}^m and l. Accordingly, any changes of them lead to the shift of the dips in the transmission fringe. From (2), the variation of λ_m, which is caused by changing the external refractive index (ERI), can be represented as:

$$\Delta\lambda_m = \frac{2l(\Delta n_{eff}^m + \Delta n)}{2m+1} - \frac{2l\Delta n_{eff}^m}{2m+1} = \frac{2l\Delta n}{2m+1} \tag{3}$$

where Δn is the fluctuation of Δn_{eff}^m. In fact, the sensor functionality is justified by the wavelength modulation. The operation principle of the MSM fiber structure is based on modal interference between the core mode and the excited high-order modes propagating through the SMF segment. Free spectrum range (FSR), the distance between two adjacent interference dips, can be approximated as [6,26]:

$$\left|\Delta\lambda_{FSR}\right| = \left|\lambda_{m+1} - \lambda_m\right| \simeq \frac{\lambda_m^2}{l\Delta n_{eff}^m} \tag{4}$$

The length of the SMF section affects the final shape of the spectrum; thus, the longer the l, the shorter the distance between dips, resulting in the compact spectrum.

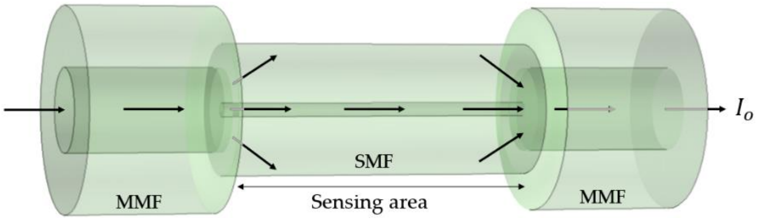

Figure 1. The schematic diagram of the MESM fiber

To fabricate the sensors, standard step-index single-mode and multimode fibers are prepared in which the core diameters are 8.2 and 50 µm, respectively, and the outer diameter of both is 125µm. After removing the protective coatings, their cross-section is cut vertically using a cleaver and welded together by a fusion splicing machine (Sumitomo T55). In this way, specific lengths of the SMF are connected between two multimode pigtails, creating the MSM structure .To reduce the diameter of the middle segment, a chemical etching method is utilized, so each structure is etched in pure hydrofluoric acid (40%) at room temperature. The etching process is performed at a fixed time of 47 minutes. The residual fiber diameters (RFDs) of some samples of structures are given in Table 1, which shows that the fabrication process has almost good reproducibility. To investigate the SPR effect on the MSM and MESM sensor performance, a thin Au film of 20, 35, and 55 nm thicknesses are deposited on one side of the sensing area of the structures by using the sputter coating method. Schematic structures of the fabricated sensors–MSM, MESM, MSM-SPR, and MESM-SPR–are shown in Figure 2.

Table 1. RFDs of several etched MESM samples

Sample	1	2	3	4	5
RFD (µm)	78.707	78.414	79.445	78.757	78.256

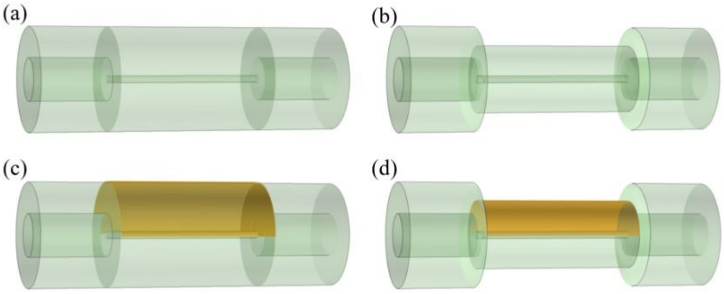

Figure 2. Schematic structures of the sensors (a) MSM, (b) MESM, (c) MSM-SPR, and (d) MESM-SPR

3. Results and Discussion

The experimental sensing setup to measure output spectra is depicted in Figure 3. The arrangement includes an optical source, optical spectrum analyzer (OSA), fiber sensors, water-glycerol solutions, and a PC. The employed broadband sources (BBSs) are Avalight-HAL-S and Avalight-DHS containing halogen lamps with wavelengths of 360 nm to 2000 nm and 360 nm to 1500 nm, respectively. The adopted spectrometers are Avaspec-NIR256-1.7 with the resolution of 5-30 nm and Avaspec-3648 with the resolution of 0.025-0.20 nm, which have operating wavelengths of 1000 nm to 1700 nm and 200 nm to 1100 nm, respectively. When the signal from the BBS enters the MSM fiber, the main mode propagates through the core of the SMF and the rest of the signal penetrates the cladding. The modes passing through these two optical paths are recombined in the second MMF, and the final interference spectrum received by the OSA is displayed on the PC. The sensing region is firmly clamped and immersed in water-glycerol solutions with different RIs. The solutions contain different weight percentages of glycerol dissolved in water (RI=1.333), and accordingly, the more the glycerol concentration (C), the more the RI becomes. Table 2 presents the RI corresponding to solutions (n_x) containing certain weight percentages of glycerol, which is measured with Abbe refractometer.

In Figure 4, the output spectra of the fabricated MSM fibers with different lengths of 2, 4, and 8 cm are demonstrated. As observed, the longer length of MSM results in smaller FSR which is consistent with theory. The inhomogeneity of patterns indicates the participation of more than two excited modes in the interference.

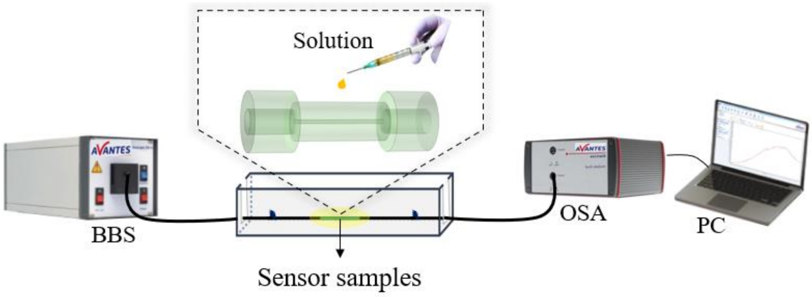

Figure 3. The experimental sensing setup to measure output spectra. The inset shows the procedure of applying the solution to be sensed on the middle segment of the MSM.

Table 2. RIs of solutions containing different concentrations of glycerol

C %	5	10	15	20	25	30	35	40	45	50
n_x	1.338	1.344	1.351	1.357	1.364	1.370	1.3577	1.384	1.390	1.398
C %	55	60	65	70	75	80	85	90	95	100
n_x	1.405	1.412	1.420	1.427	1.435	1.442	1.450	1.458	1.465	1.473

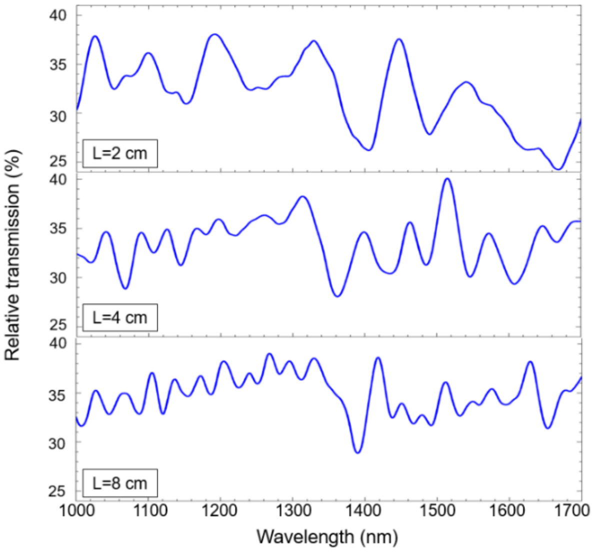

Figure 4. Measured spectra of the MSM-MZI with different lengths of the SMF

Figure 5 (a) shows the transmission spectra of the MSM fiber sensor with l=2 cm when exposed to various solutions. Experiments are performed at room temperature, and the outputs are plotted for each external refractive index (ERI) relative to the spectrum in the air. We investigate the changes of two valleys marked as Dip 1 and Dip 2 in the interference patterns. According to Figure 5 (a), the wavelengths of the dips undergo a redshift as the ERI increases. An increase in ERI has a significant effect on the field distribution of high-order modes, as the penetration of the mode field increases and a noticeable part of modes concentrates outside the fiber [27]. In other words, increasing the ERI leads to a decrease in the power of the high-order modes within the fiber [24,25,28]. Thus, the corresponding $n_{cl,eff}^{m}$ decreases as it is strongly dependent on the distribution of the mode field. According to (2), the interference dip wavelength increases, and the redshift occurs. Figure 5 (b) demonstrates the wavelength variations of both dips as a function of the ERI. According to the definition of sensitivity given by $S = d\lambda / dn_x$, when the RI varies from 1.428 to 1.458, the sensitivities of Dip1 and Dip2 are obtained as 637.71 nm/RIU and 886.85 nm/RIU, respectively.

As shown in Figure 5 (a), in addition to the wavelength, the intensity of the output signal is also modulated by changing the ERI. This behavior can also be employed in sensing analysis. Figure 6 shows the diagram of the output intensity with respect to the ERI for Dip1 and Dip2. The intensity response of the sensor is not uniform throughout the RI range denoted as Zone 1 and 2. In MSM fiber structure, the clad and the surrounding media including the solution can be considered as two layers with $\theta_c = \sin^{-1}(n_x/n_{cl})$, where n_{cl} and n_x are the RI of the clad and solution, respectively. The cladding modes are confined inside it, and while propagating and reaching the fiber-environment boundary, a small amount of output power loss is achieved, which happens due to the generation of EWs at the interface (Zone 1). In Zone 2, as n_x increases and approaches n_{cl}, $\theta'_c = \sin^{-1}(n_x/n_{cl})$ gets larger, and a greater amount of the beam enters the fiber environment (the solution). As a result, the leakage of the modes to the outside increases, leading to a severe drop in signal strength. There is still a field leakage due to the EW, but its effect on the great loss is minimal. It should be noted that for n_x equal to or even greater than n_{cl}, the output power level never becomes zero because only cladding modes are affected by environmental changes, and the SMF core mode is always trapped and propagates without any change. According to Figure 6, the slope of the power drop versus the RI in Zone 2 can be approximated as -1541.81 %/RIU and -1613.81 %/RIU in the range of 1.428 to 1.465 for Dip 1 and Dip 2, respectively.

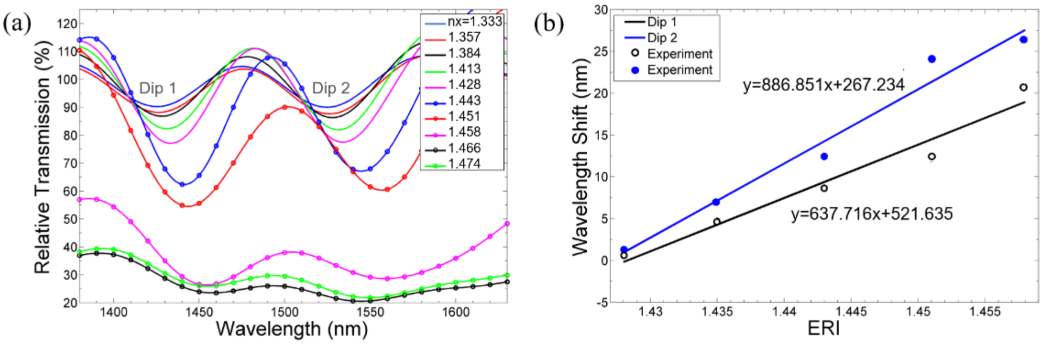

Figure 5. (a) Transmission spectra of an MSM-MZI sensor immersed in solutions with different refraction indices, (b) The measured wavelength shift of interference dips versus ERI

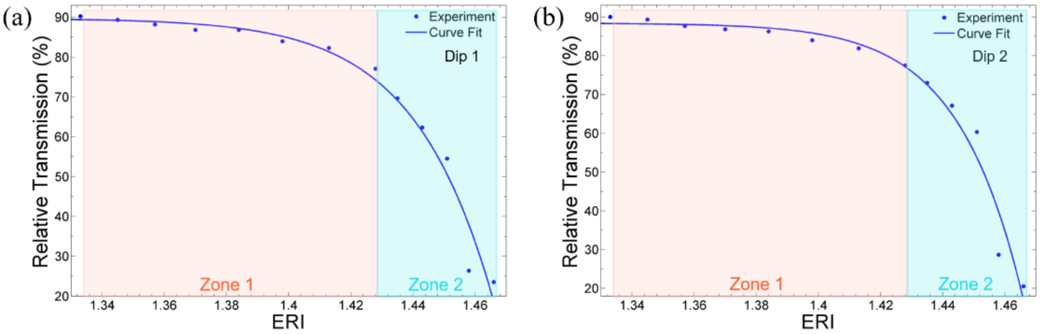

Figure 6. The variations of the output power with the ERI changes for (a) Dip 1 and (b) Dip 2

To investigate the effect of reducing the diameter of the sensing area, the experiments are repeated for the etched structure (MESM). The MESM RI responses for the interference dip around 1440 nm are exhibited in Figure 7. As explained before, both wavelength shift and intensity analysis versus ERI are investigated. The sensitivities of 1313.14 nm/RIU and -2308.92 %/RIU are achieved in the RI range of 1.428-1.458, which is clearly improved (about 50%) compared to that of the MSM sensor. Reducing the diameter of the sensitive area leads to a considerable increase in the interaction between the cladding modes and the surrounding media. As a result, the etched structure receives more ERI changes and causes a better sensitivity.

To increase the sensitivity of the device we utilized the structures with the SPR effect as depicted in Figure 2 (c) and (d). The interaction between the EWs created at the fiber-gold interface, and the surface plasmon waves (SPWs) at the surface of the metal layer is required for the formation of the SPR. Parameters such as the Au thickness and the RI of the external environment affect the SPR spectrum. The output SPR spectra of the MESMs coated with gold thicknesses of 20, 35, and 55 nm are plotted in Figure 8. The results show the transmission spectra of devices when they are immersed in water with respect to the air. Since the evanescent field has a certain penetration depth, as the thickness of the gold layer increases, EW does not reach the interface of the Au-solution to induce the SPR effect. So, the depth of the resonance dip decreases or even the dip disappears as the thickness of the gold increases. Furthermore, the thicker gold layer results in the redshift of the plasmon resonance wavelength (λ_r) which is defined as the wavelength with the minimum reflection coefficient [29].

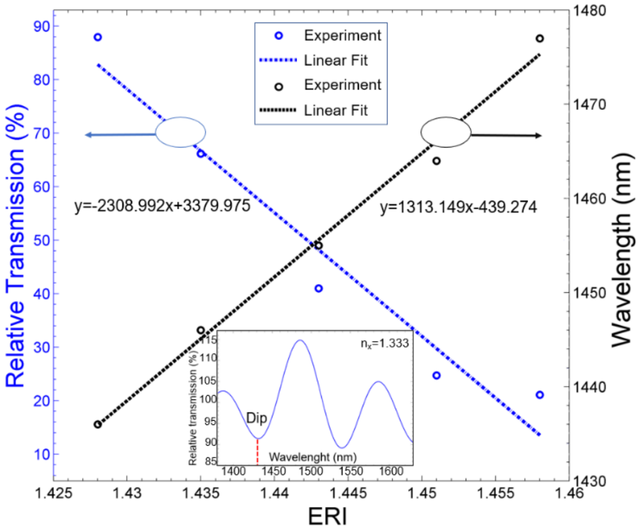

Figure 7. RI sensitivity based on intensity and wavelength interrogation for the MESM sensor. The dip around 1440 nm where the investigations have been performed is marked in the inset.

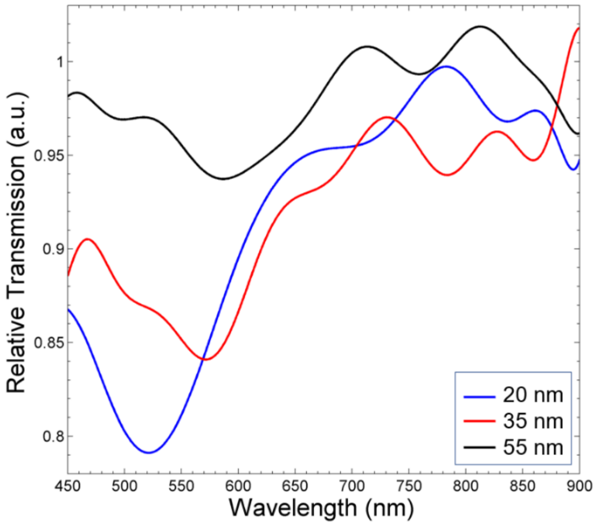

Figure 8. SPR transmission spectra of the MESM fibers coated with different Au film thicknesses

Figure 9 (a)-(c) show the SPR spectra of MESM sensors whose sensitive regions are coated with gold thicknesses of 20, 35, and 55 nm, and are exposed to solutions with different RIs. The length of the SMF is considered to be 2 cm. All of the output spectra are plotted relative to the one in the air. As observed in all the figures, increasing the ERI leads to a red-shift in λ_r. Figure 9 (d) shows the variation of the resonance wavelength versus different ERIs for the sensors. The best sensitivity is 1233 nm/RIU in the RI range of 1.333-1.371, which is calculated as the ratio of λ_r changes against the ERI variations and belongs to the sensor coated with 35 nm Au layer.

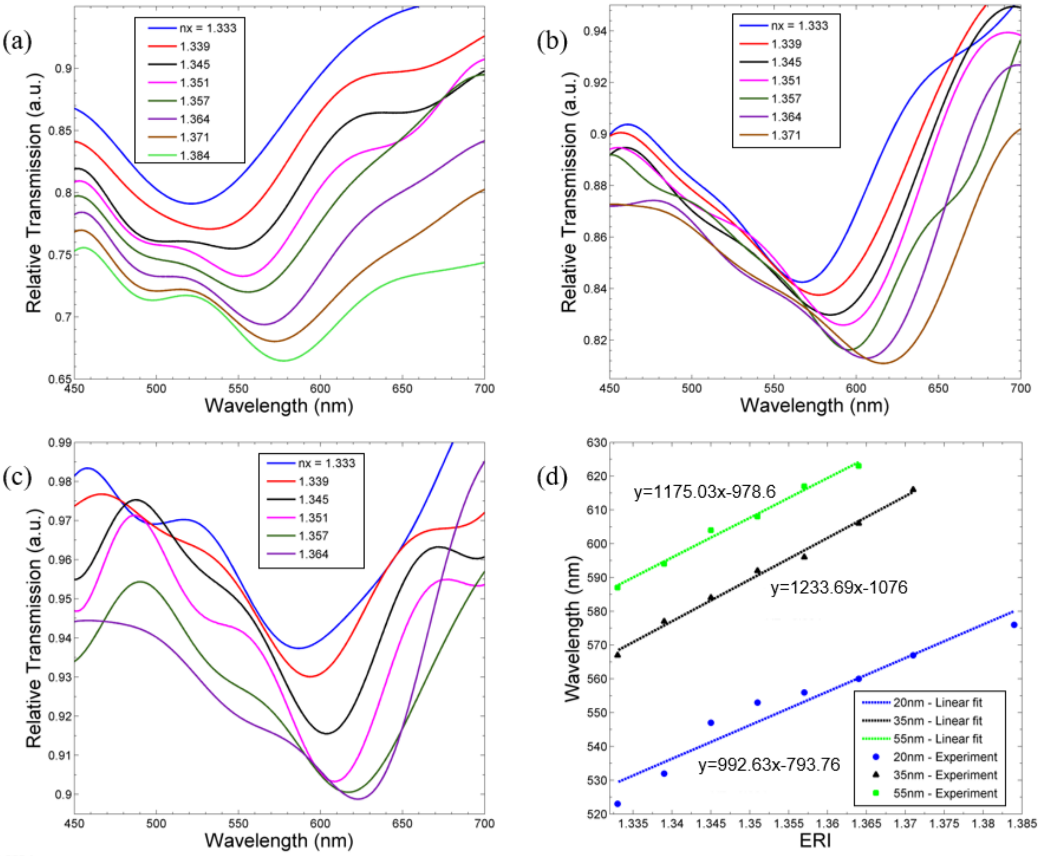

Figure 9. The SPR spectra of the MESM fiber coated with gold thicknesses of (a) 20, (b) 35, and (c) 55 nm. (d) the shift of the resonance wavelength with ERI variation for all the sensors

Figure 10 shows the results of the SPR dip wavelength shifts with respect to the ERI for MSM-SPR and MESM-SPR sensors where the sensitive region length and the gold thickness are 4 cm and 35 nm, respectively. The black curve corresponds to the unetched structure and the blue curve is related to the etched one. The sensitivities of 917.65 nm/RIU and 1433.33 nm/RIU when the ERI varies from 1.333 to 1.357 are achieved for MSM-SPR and MESM-SPR sensors, respectively. It is clear that similar to the aforementioned results of MSM and MESM sensors, reducing the diameter of the sensitive area is fairly effective in improving the sensitivity. Regarding the high sensitivity achieved for the MESM-SPR fiber sensor, they can be considered as very promising sensors for different applications.

A comparison of the sensing performance between several RI fiber sensors is listed in Table 3. As can be seen, our proposed sensors have a high sensitivity over a wide operational range. Hence, reducing the waist of the sensing region and the combination of MZI as well as SPR significantly improve the performance of the proposed fiber sensors.

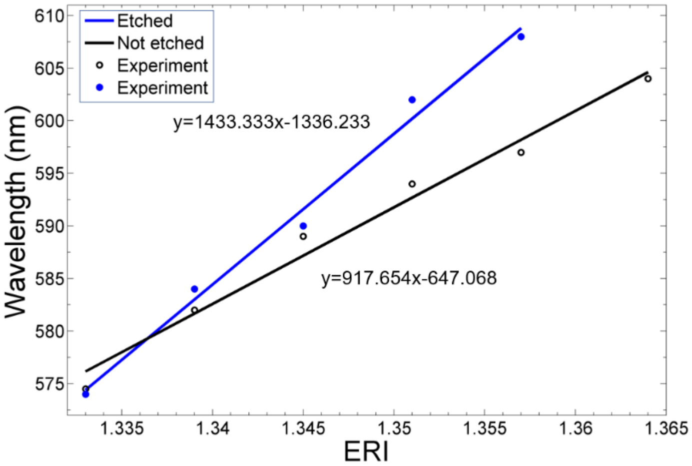

Figure 10. Comparison of the resonance wavelength shift of the MSM-SPR and MESM-SPR sensors

Table 3. Comparison of the proposed sensors with the other reported RI sensors

Sensor structure	Sensing mechanism	Sensitivity (nm /RIU)	Dynamic range
MESM (This work)	MZI	1313	1.428-1.458
MESM-SPR (This work)	MZI and SPR	1433	1.333-1.357
MMF-no-core fiber [30]	MZI	1191.5	1.3405-1.3497
SMF-THOF-SMF [31]	MZI	7041.21	1.4406-1.4456
SM-PC-SM fiber [21]	MZI	260.8	1.3333-1.3737
Tapered MSM [23]	MZI	1879.87	at 1.437
S-tapered fiber [32]	MZI	1882.4	1.4216-1.4284
Front- tapered SMS [9]	MZI and MMI	82.58	1.330-1.370
Tapered coreless fiber [12]	MMI and SPR	866.1	1.3864-1.416
Tapered fiber [33]	LSPR	892	1.333-1.380
U-bent POF [34]	LSPR	700.3	1.330-1.3657
MSM [35]	MZI and SPR	765.1	1.333-1.365

LSPR = Localized surface plasmon resonance, THOF = Tapered hollow optical fiber, POF = Plastic optical fiber.

4. Conclusions

In summary, four RI fiber sensor structures comprising MSM, MESM, MSM-SPR, and MESM-SPR are fabricated and studied. All the sensors are based on the MZI structure formed by splicing an SMF section between two MMFs. The chemical etching technique is applied to reduce the cladding diameter of the sensing area, and Au coating is performed to benefit from the SPR feature. Simultaneous use of SPR effect and chemical etching provides a high-performance Mach-Zehnder RI sensor. According to the experimental results, the etched structure-based sensors show better sensitivity to ERI variations due to the increase of light interaction with the environment. By changing the RI from 1.428 to 1.458, the MESM sensor possesses the best sensitivity of -2308.92 %/RIU and 1313.14 nm/RIU; additionally, the MESM-SPR has the best sensitivity of 1433.33 nm/RIU in the dynamic RI range of 1.333-1.357. Due to the facile and low-cost process of fabrication of the proposed sensors, as well as their high sensitivity and reproducibility, they are considered as efficient and useful devices in several applications like the food industry, biosensing, and chemical applications.

Author Contributions: Conceptualization, Z.A. and V.A.; methodology, Z.A.; validation, Z.A. and V.A.; formal analysis, Z.A. and V.A.; investigation, Z.A.; data curation, Z.A.; writing—original draft

preparation, Z.A.; writing—review and editing, V.A and F.A.; supervision, V.A.; funding acquisition, V.A. All authors have read and agreed to the published version of the manuscript.

Funding: This research was funded by Iran National Science Foundation (INSF) and Tarbiat Modares University (Grant No. IG-39703).

Institutional Review Board Statement: Not applicable.

Informed Consent Statement: Not applicable.

Acknowledgments: Ms. Zahra Akbarpour would like to thank Mr. Saeid Gerami for his support and help throughout the project.

Conflicts of Interest: The authors declare no conflict of interest.

References

1. Apriyanto, H.; Ravet, G.; Bernal, O.D.; Cattoen, M.; Seat, H.C.; Chavagnac, V.; Surre, F.; Sharp, J.H. Comprehensive modeling of multimode fiber sensors for refractive index measurement and experimental validation. *Sci. Rep.* **2018**, *8*, 1-13. [CrossRef]
2. Yasin, M.; Arof, H.; Harun, S.W. Optical fiber sensors: An overview. In *Fiber Optic Sensors*, InTech: Croatia, Europe, 2012; pp. 1-52.
3. Lee, B.H.; Kim, Y.H.; Park, K.S.; Eom, J.B.; Kim, M.J.; Rho, B.S.; Choi, H.Y. Interferometric fiber optic sensors. *Sensors* **2012**, *12*, 2467-2486. [CrossRef]
4. Krohn, D.A.; MacDougall, T.; Mendez, A. Fiber optic sensor fundamentals. In *Fiber Optic Sensors: Fundamentals and Applications*, 4th ed.; SPIE: Bellingham, Washington, USA, 2014; pp. 21-30.
5. Dong, X.; Du, H.; Luo, Z.; Duan, J. Highly sensitive strain sensor based on a novel Mach-Zehnder interferometer with TCF-PCF structure. *Sensors* **2018**, *18*, 278. [CrossRef]
6. Dong, X.; Luo, Z.; Du, H.; Sun, X.; Yin, K.; Duan, J. Highly sensitive strain sensor based on a novel Mach–Zehnder mode interferometer with TCF-PCF-TCF structure. *Opt. Lasers Eng.* **2019**, *116*, 26-31. [CrossRef]
7. Xian, P.; Feng, G.; Ju, Y.; Zhang, W.; Zhou, S. Single-mode all-fiber structured modal interference for temperature and refractive index sensing. *Laser Phys. Lett.* **2017**, *14*, 085101. [CrossRef]
8. Yin, B.; Li, Y.; Liu, Z.B.; Feng, S.; Bai, Y.; Xu, Y.; Jian, S. Investigation on a compact in-line multimode-single-mode-multimode fiber structure. *Opt. Laser Technol.* **2016**, *80*, 16-21. [CrossRef]
9. Kang, J.; Yang, J.; Zhang, X.; Liu, C.; Wang, L. Intensity demodulated refractive index sensor based on front-tapered single-mode-multimode-single-mode fiber structure. *Sensors* **2018**, *18*, 2396. [CrossRef]
10. Li, C.; Ning, T.; Zhang, C.; Li, J.; Zhang, C.; Wen, X.; Lin, H.; Pei, L. All-fiber multipath Mach-Zehnder interferometer based on a four-core fiber for sensing applications. *Sens. Actuator A Phys.* **2016**, *248*, 148-154. [CrossRef]
11. Mumtaz, F.; Dai, Y.; Ashraf, M.A. Inter-cross de-modulated refractive index and temperature sensor by an etched multi-core fiber of an MZI structure. *J. Lightwave Technol.* **2020**, *38*, 6948-6953. [CrossRef]
12. Ding, Z.W.; Lang, T.T.; Wang, Y.; Zhao, C.L. Surface plasmon resonance refractive index sensor based on tapered coreless optical fiber structure. *J. Lightwave Technol.* **2017**, *35*, 4734-4739. [CrossRef]
13. Liu, Y.; Li, S.; Chen, H.; Li, J.; Zhang, W.; Wang, M. Surface plasmon resonance induced high sensitivity temperature and refractive index sensor based on evanescent field enhanced photonic crystal fiber. *J. Lightwave Technol.* **2019**, *38*, 919-928. [CrossRef]
14. Zhao, J.; Cao, S.; Liao, C.; Wang, Y.; Wang, G.; Xu, X.; Fu, C.; Xu, G.; Lian, J.; Wang, Y. Surface plasmon resonance refractive sensor based on silver-coated side-polished fiber. *Sens. Actuators B Chem.* **2016**, *230*, 206-211. [CrossRef]
15. Allsop, T.; Neal, R. A review: Evolution and diversity of optical fiber plasmonic sensors. *Sensors* **2019**, *19*, 4874. [CrossRef]
16. G. C. Righini, A. Tajani, and A. Cutolo, Surface plasmon resonance: applications in sensors and biosensors. In *An Introduction to Optoelectronic Sensors*, World Scientific: Singapore, 2009; Volume 7, pp. 111-125.
17. Roh, S.; Chung, T.; Lee, B. Overview of the characteristics of micro-and nano-structured surface plasmon resonance sensors. *Sensors* **2011**, *11*, 1565-1588. [CrossRef]
18. Gandhi, M.; Chu, S.; Senthilnathan, K.; Babu, P.R.; Nakkeeran, K.; Li, Q. Recent advances in plasmonic sensor-based fiber optic probes for biological applications. *Appl. Sci.* **2019**, *9*, 949. [CrossRef]
19. Gu, M.; Yuan, S.; Yuan, Q.; Tong, Z. Temperature-independent refractive index sensor based on fiber Bragg grating and spherical-shape structure. *Opt. Lasers Eng.* **2019**, *115*, 86-89. [CrossRef]
20. Urrutia, A.; Villar, I.D.; Zubiate, P.; Zamarreño, C.R. A comprehensive review of optical fiber refractometers: Toward a standard comparative criterion. *Laser Photonics Rev.* **2019**, *13*, 1900094. [CrossRef]
21. Wang, Q.; Kong, L.; Dang, Y.; Xia, F.; Zhang, Y.; Zhao, Y.; Hu, H.; Li, J. High sensitivity refractive index sensor based on splicing points tapered SMF-PCF-SMF structure Mach-Zehnder mode interferometer. *Sens. Actuators B Chem.* **2016**, *225*, 213-220. [CrossRef]
22. Du, H.; Sun, X.; Hu, Y.; Dong, X.; Zhou, J. High sensitive refractive index sensor based on cladding etched photonic crystal fiber Mach-Zehnder interferometer. *Photonic Sens.* **2019**, *9*, 126-134. [CrossRef]

23. Zhang, S.; Wang, Z.; Zhu, M.; Li, L.; Wang, S.; Li, S.; Peng, F.; Niu, H.; Li, X.; Deng, S.; Geng, T.; Yang, W.; Yuan, L. A compact refractive index sensor with high sensitivity based on multimode interference. *Sens. Actuator A Phys.* **2020**, *315*, 112360. [CrossRef]
24. Zhang, R.; Pu, S.; Li, Y.; Zhao, Y.; Jia, Z.; Yao, J.; Li, Y. Mach-Zehnder interferometer cascaded with FBG for simultaneous measurement of magnetic field and temperature. *IEEE Sens. J.* **2019**, *19*, 4079-4083. [CrossRef]
25. Tang, J.; Pu, S.; Dong, S.; Luo, L. Magnetic field sensing based on magnetic-fluid-clad multimode-single mode-multimode fiber structures. *Sensors* **2014**, *14*, 19086-19094. [CrossRef]
26. Ma, Y.; Qiao, X.; Guo, T.; Wang, R.; Zhang, J.; Weng, Y.; Rong, Q.; Hu, M.; Feng, Z. Mach–Zehnder interferometer based on a sandwich fiber structure for refractive index measurement. *IEEE Sens. J.* **2012**, *12*, 2081-2085. [CrossRef]
27. Yang, R.; Yu, Y.S.; Xue, Y.; Chen, C.; Chen, Q.D.; Sun, H.B. Single S-tapered fiber Mach–Zehnder interferometers. *Opt. Lett.* **2011**, *36*, 4482-4484. [CrossRef]
28. Dong, S.; Pu, S.; Wang, H. Magnetic field sensing based on magnetic-fluid-clad fiber-optic structure with taper-like and lateral-offset fusion splicing. *Opt. Express* **2014**, *22*, 19108-19116. [CrossRef]
29. Zhang, Z.; Chu, F.; Guo, Z.; Fan, J.; Li, G.; Cheng, W. Design and optimization of surface plasmon resonance sensor based on polymer-tipped optical fiber. *J. Lightwave Technol.* **2018**, *37*, 2820-2827. [CrossRef]
30. Wang, F.; Pang, K.; Ma, T.; Wang, X.; Liu, Y. Folded-tapered multimode-no-core fiber sensor for simultaneous measurement of refractive index and temperature. *Opt. Laser Technol.* **2020**, *130*, 106333. [CrossRef]
31. Zhu, C.C.; Yu, Y.S.; Zhang, X.Y.; Chen, C.; Liang, J.F.; Liu, Z.J.; Meng, A.H.; Jing, S.M.; Sun, H.B. Compact Mach–Zehnder interferometer based on tapered hollow optical fiber. *IEEE Photon. Technol. Lett.* **2015**, *27*, 1277-1280. [CrossRef]
32. Chen, C.; Yang, R.; Zhang, X.Y.; Wei, W.H.; Guo, Q.; Zhang, X.; Qin, L.; Ning, Y.Q.; Yu, Y.S. Compact refractive index sensor based on an S-tapered fiber probe. *Opt. Mater. Express* **2018**, *8*, 919-925. [CrossRef]
33. Wieduwilt, T.; Zeisberger, M.; Thiele, M.; Doherty, B.; Chemnitz, M.; Csaki, A.; Fritzsche, W.; Schmidt, M.A. Gold-reinforced silver nanoprisms on optical fiber tapers—A new base for high precision sensing. *APL Photonics* **2016**, *1*, 066102. [CrossRef]
34. Jiang, S.; Li, Z.; Zhang, C.; Gao, S.; Li, Z.; Qiu, H.; Li, C.; Yang, C.; Liu, M.; Liu, Y. A novel U-bent plastic optical fibre local surface plasmon resonance sensor based on a graphene and silver nanoparticle hybrid structure. *J. Phys. D Appl. Phys.* **2017**, *50*, 165105. [CrossRef]
35. García, J.A.; Monzón-Hernández, D.; Manríquez, J.; Bustos, E. One step method to attach gold nanoparticles onto the surface of an optical fiber used for refractive index sensing. *Opt. Mater.* **2016**, *51*, 208-212. [CrossRef]